A rapid scan vacuum FTIR method for determining diffusion coefficients in viscous and glassy aerosol particles

Yun Zhang[1], Chen Cai[1,3], Shu-Feng Pang[1], Jonathan P. Reid[2], Yun-Hong Zhang[1]*

[1]*Institute for Chemical Physics, Beijing Institute of Technology, Beijing 100081, People's Republic of China*

[2]*School of Chemistry, University of Bristol, Bristol BS8 1TS, United Kingdom*

[3]*Department of Atmospheric and Oceanic Sciences, School of Physics, Peking University, Beijing 100871*

Graphic abstract

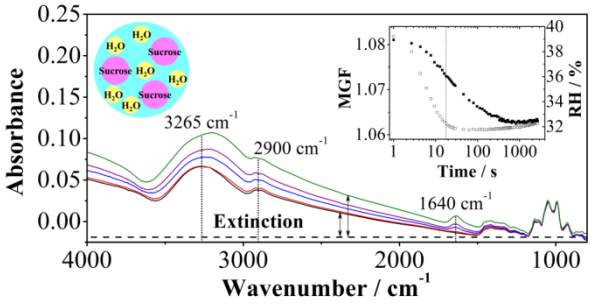

Abstract

We report a new method to investigate water transport kinetics in aerosol particles by using rapid scan FTIR spectroscopy combined with a custom-built pulse relative humidity (RH) control system. From real time in situ measurements of RH and composition using high time resolution infrared spectroscopy (0.12 s for one spectrum), and through achieving a high rate of RH change (as fast as 60% per second), we are able to investigate the competition between the gas and condensed phase diffusive transport limits of water for particles with mean diameter ~3 μm and varying phase and viscosity. The characteristic time (τ) for equilibration in particle composition following a step change in RH is measured to quantify dissolution timescales for crystalline particles and to probe the kinetics of water evaporation and condensation in amorphous particles. We show that dissolution kinetics are prompt for crystalline inorganic salt particles following an increase in RH from below to above the deliquescence RH, occurring on a timescale comparable to the timescale of the RH change (<1 s). For aqueous sucrose particles, we show that the timescales for both the drying and condensation processes can be delayed by many orders of magnitude, depending on the viscosity of the particles in the range 10^1 to 10^9 Pa·s considered here. For amorphous particles, these kinetics are shown to be consistent with previous measurements of

mass transfer rates in larger single particles. More specifically, the consistency suggests that fully understanding and modelling the complex microphysical processes and heterogeneities that form in viscous particles may not be necessary for estimating timescales for particle equilibration. A comparison of the kinetics for crystalline and amorphous particles illustrates the interplay of the rates of gas and condensed phase diffusion in determining mass transport rates of water in aerosol.

1. Introduction

Atmospheric aerosols affect the earth's climate directly by scattering and absorbing radiation, and indirectly by influencing cloud formation as cloud condensation nuclei.[1-7] The uncertainty associated with the combined magnitude of radiative forcing from aerosol is recognized as large, at part because of a poor understanding of the physical and chemical properties of aerosols.[8-10] Hygroscopicity is an important property of aerosols, impacting on aerosol particle size and composition, influencing aerosol phase chemical reactions, and affecting optical properties.[11,12] Many thermodynamic models have been developed to estimate the equilibrium partitioning of water and semi-volatile organic components between the gas and condensed phases in atmospheric aerosols.[13-18] However, an assumption that thermodynamic equilibrium is always achieved may not be correct when predicting the properties of viscous or amorphous aerosols due to slow mass transport rates arising from slow bulk-phase diffusion. Diffusion in the particle bulk phase could also influence the composition of aerosols, particularly the partitioning of semi-volatile organic compounds between the gas and condensed phases.[19]

The proportion of organic components in atmospheric aerosol can be as high as 30% to 80% of total aerosol mass.[20,21] The organic-rich phase of atmospheric aerosols can be classified as a liquid ($\eta < 10^2$ Pa·s; where η is the dynamic viscosity), a semi-solid (10^2 Pa·s $< \eta <$ 10^{12} Pa·s) or a solid ($\eta > 10^{12}$ Pa·s), depending on ambient conditions and chemical composition.[22-25] Indeed, Virtanen et al. showed that secondary organic aerosol (SOA) could exist in a glassy phase, while other studies suggest that aerosol particles could be characterised as gels or rubbers.[26-29] Based on the relationship between viscosity and diffusion constant suggested by the Stokes-Einstein equation, it might be expected that diffusion constants could be characterised by a similarly wide range, depending on the viscosity and phase of the aerosol.[24] Such variation could lead to an underestimate of the observed aerosol total mass and substantial uncertainties in predicted radiative forcing of atmospheric aerosols.[21,27,30-32] Thus, obtaining accurate kinetic parameters is essential to estimate the time scale for aerosols to response to changes of environment conditions.

Recently, new experimental methods have been developed to study the diffusion of small molecules in aerosol particles and their relationship to bulk phase viscosity.[24,33-38] Shiraiwa et al.[24] used a coated wall flow tube to measure the ozone uptake by amorphous protein over wide ranges of ozone concentration and RH, and observed a diffusion limited ozone uptake and oxidative

reaction in amorphous protein. With the electro-dynamic balance method, Zobrist et al.[34] measured the water uptake and release from a single micrometre-sized aqueous sucrose droplet with change of ambient temperature and humidity. These kinetic measurements led to a parameterization of diffusion coefficient of water as a function of RH and temperature in sucrose aerosol, showing variation by more than 10 orders of magnitude with environmental conditions.[40,41] This method has now been used to measure water transport kinetics in SOA samples.[42] Pope et al.[43-46] use fluorescence lifetime imaging to study the microscopic viscosity of organic aerosol undergoing chemical aging. In measurements on optically trapped droplets, they reported an increase in viscosity of squalene droplets upon ozonolysis, with the viscosity range of ~5000 mPa s - ~10^{14} mPa s. Price et al.[38-40] have developed a confocal Raman approach to infer diffusion constants by following with spatial resolution the exchange of H_2O by D_2O in a sample of cylindrical symmetry, reporting diffusion constants of water in sucrose and SOA samples.

To approach the problem of amorphous aerosol phases from the perspective of viscosity rather than diffusion constant measurements, holographic optical tweezers have been used to measure the viscosity of micro-particles over a range of 12 orders of magnitude for aqueous-sucrose particles.[35] Diffusion constant calculated from these viscosities using the Stokes-Einstein equation showed large differences to the value directly determined by Zobrist et al.[34] for highly viscous droplets. Considering the importance of directly investigating diffusion in highly viscous aerosols for understanding the physical and chemical properties of atmospheric aerosols, there is a need for complementary techniques with high time-resolution and sensitivity.

We report here an experimental technique combining rapid scan FTIR spectroscopy with a pulsed RH control system to measure the timescale for dissolution of crystalline particles and water diffusion constants in amorphous particles deposited on a substrate. Previously, we have studied mass transfer processes controlled by bulk phase and surface processes in magnesium sulphate and magnesium nitrate aerosols.[47] In this work, time resolved FTIR spectra of inorganic salt particles and sucrose solution particles are reported during a rapid step change in RH (<0.1 s). The RH of the gas phase is inferred extremely accurately from the changing intensity of gas phase absorption lines. From these spectra, time-dependent mass growth factors of initially crystalline or amorphous particles are determined by quantitative analysis of the condensed phase water band area in each spectrum. From these experiments, we explore the interplay of gas and condensed

phase diffusional transport in determining the kinetics of condensation and evaporation of water from crystalline and amorphous particles.

2. Experimental Description

2.1. Experimental apparatus

A schematic diagram of the vacuum FTIR experimental setup is shown in Figure 1. The sample chamber is a 12 cm length cylinder with an inner diameter of 2.5 cm. It is located inside the sample compartment of FTIR spectrometer. Detachable zinc selenide (ZnSe) or calcium fluoride (CaF_2) hermetically sealed windows are installed at the two ends of the cylinder. The windows seal the sample chamber as well as allowing the IR beam to pass through. The sample chamber is connected to a pump (2XZ-2B, Shanghai) and water reservoir. Ultrapure water (18.25 MΩ·cm, ULUPURE, Xi'an) in the reservoir provides the source of water vapour. A thermostatic water bath is used to keep the temperature of water constant. The water vapour pressure in the sample chamber is controlled by two valves and two taps. The RH and pressure of the sample chamber environment are measured by a humidity sensor (Dwyer HU1142, ±2% RH) and a differential pressure transmitter (Rosemount 3051, accuracy>0.5%), respectively. The valves, humidity probe and pressure metre are controlled by a program which also collects the experimental data.

During the measurement, the sample chamber was first evacuated to around 0.01 kPa to collect the IR background spectrum. Then, aerosol particles were nebulized from bulk solution and deposited on the ZnSe or CaF_2 windows. The images of deposited aerosols shown in Figure 2(a) were observed by an optical microscope (XSP-BM, Shanghai) and recorded by a digital camera (Nikon-5700). Then, the windows were re-installed onto the sample chamber. The chamber was connected to the vacuum pump and evacuated to a pressure of 0.01kPa. By controlling taps and valves, the water vapour pressure in the sample chamber was varied, changing to a required value and at a particular rate. FTIR spectra were collected synchronously during the change in RH. From the vapour phase signals in the IR spectra, the RH was acquired in real-time. Further, from the broad underlying condensed phase signatures, the average particle composition was acquired synchronously. The analyses of these is described in greater detail later.

FTIR spectra were recorded by a Vacuum FTIR spectrometer (Bruker, Vertex 80v) with a liquid nitrogen cooled MCT detector. During the experiment, the interferometer compartment and

sample compartment of the spectrometer were evacuated to less than 0.21 kPa by using a pump (Adixen, ACP 15) to remove water vapour and CO_2 in the IR beam path. The scan rate of interferometer can be controlled. In rapid-scan mode, the scan frequency is set as 160 kHz to record 9 spectra per second at spectral resolution of 4 cm^{-1}. In low speed scan mode, the scan frequency is set as 20 kHz and each spectrum is the average of 16 scans to provide higher signal-to-noise ratio spectra.

2.2. Sample preparation

An aqueous sucrose solution of 0.1 $mol \cdot L^{-1}$ (Beijing Chemical Works, A.R., prepared by using ultrapure water, 18.25 $M\Omega \cdot cm^{-1}$, from UP Water Purification System, ULUPUER, Xi'an) was used to produce droplets from an ultrasonic nebulizer, for deposition onto the ZnSe or CaF_2 windows. The deposited dry particles were in the size range from hundreds nanometres to several micrometres according to the images recorded by camera. A typical size distribution of particles deposited on the substrate is illustrated in Figure 2(b) along with the corresponding mass distribution in Figure 2(c) and contact area distribution on Figure 2(d). Around 70% of the particles were in the range ~1 μm to ~3 μm.

2.3. Measurements of the RH in real-time from FTIR spectra

According to Beer-Lambert's law,

$$A_\nu = \varepsilon_\nu bc \qquad (1)$$

where A_ν is the absorbance at wavenumber ν, ε_ν is the molar absorption coefficient ($dm^3 \cdot cm^{-1} \cdot mol^{-1}$), L is the optical path length (cm) and c is the concentration of sample ($mol \cdot dm^{-3}$).

For water vapour at room temperature (298 K), the vapour is assumed to behave as an ideal gas, thus,

$$A_\nu = \varepsilon_\nu Lc = p \cdot \frac{\varepsilon_\nu L}{RT} \qquad (2)$$

The RH is defined as

$$RH = \frac{p}{p_0} \times 100 \qquad (3)$$

Given the gas phase is composed of just water at varying pressure, these equations together can be written as

$$A_\nu = k \cdot RH \qquad (4)$$

where,

$$k = \frac{\varepsilon_\nu L p_0}{RT} \qquad (5)$$

in which L is the length of sample cell and ε_ν is the molar absorption coefficient of water vapour. In the present experiment, the peak area of two strong ro-vibrational transitions in a vibration band is used to estimate the RH based on a prior calibration. Thus, differences of ε_ν of different ro-vibrational transition in the IR band are not important in the RH determination although different ro-vibrational transitions could be used in principle to determine both the temperature and RH in the cell without calibration.

In the calibration process, the saturated pressure of water vapour p_0 as a function of temperature, T, is known: at 299 K, the saturated vapour pressure of water p_0 is 3.37 kPa. Then for a sequence of IR measurements with varying partial pressure of water, p, the corresponding RH can be determined. Thus, the absorbance A_ν of a band acquired from collected FTIR spectra can be related to the RH over a range in water partial pressure, as shown in Figure 3(a). The band at 1844.2 cm^{-1} is selected to provide a measure of the RH and the linear slope k, relating A_ν to RH, can be determined, as shown in Figure 3(b). Although this band is comprised of two strong ro-vibrational transitions of water, at 1844.181 cm^{-1} and 1844.399 cm^{-1}, these are unresolved in our measurements and the combined intensity of both lines is used in the RH calibration. These lines fall in a spectroscopic window that does not overlap with the nearest condensed phase absorption band below 1700 cm^{-1}. This value of k is then adopted to calculate the value of RH during any rapid process, allowing much higher time-resolution measurements of RH from the gas phase IR spectra than could be achieved from more conventional measurements of p or RH directly.

3. Results and Discussion

3.1 Spectral Information

Spectra of sucrose aerosol particles deposited to ZnSe windows at various RHs are shown in different colours in Figure 4. The water vapour absorption bands have been removed through applying the subtraction of a reference background spectrum, as we must first subtract the presence of the gas phase lines (used to determine the RH). Inset A shows a comparison of spectra before and after the subtraction of the water vapour bands. Inset B shows the vapour peak used to

calculate RH as described in section 2.3, while Inset C shows the band area used to characterize the water content of aerosol particles. The broad band from the O-H stretching vibration is centred at 3268 cm^{-1}. The weak band around 2900 cm^{-1} is the stretching vibration absorption of $-CH_3$ and $-CH_2-$ group in the sucrose molecule. The band around 1640 cm^{-1} is assigned to the bending vibration absorption of water molecule. The bands located between 1500 cm^{-1} and 800 cm^{-1} arise from lower frequency vibration modes of sucrose and the line shapes are similar to those reported in the literature for sucrose existing as a rubber or glassy phase.[48] The non-absorbing rise in extinction with increase in wavenumber is a consequence of the increase in light scattering by the particles deposited on the substrate. As the particle size decreases with decrease in RH, this scattering component of extinction becomes weaker consistent with this change in size. In these spectra, the -OH groups in sucrose, -OH bonds in water and the interaction between water and sucrose molecules together determine the line shape and band area of the O-H stretching band; thus, this band cannot be used to determine the water content of aerosol particles quantitatively. However, the H-O-H bending vibration band can be attributed to water alone, and this band area is used to quantitatively characterize the condensed phase water content of the deposited particles, as seen in Inset C. The narrow gas phase lines falling within the integration window 1550 to 1700 cm^{-1} can readily be subtracted from the continuous condensed phase line profile. For the subtraction, we first collect a single background infrared spectrum of water vapour under the same conditions (including temperature, spectral resolution, accumulation etc.) of experimental measurements. Then we use the subtraction function in Nicolet OMNIC 8.0 software to do the subtraction between experimental spectra and single background spectrum and remove the water vapour signal from experimental spectra. In the subtraction the background spectrum is multiplied with an adjustment coefficient k, to make sure that the intensity of water vapour signal in experimental spectra and background spectrum match with each other. This leaves a signal that arises from condensed phase water alone.

3.2 Measurements of the dissolution timescales of crystalline inorganic salt particles

In section 2.3, we introduced the method for calculating RH by using water vapour FTIR spectra, and Figure 3 has shown this method is reliable when the RH is held constant. In this part, we will verify the accuracy of the RH measurement during a pulsed change in RH and use the approach to measure the dissolution timescale of crystalline particles to form solution droplets.

During a RH pulse, the RH can change as fast as 60 % s^{-1} and no humidity detector can respond so promptly. Here we assess the accuracy of the FTIR absorption method for fast RH detection. First, the RH was increased slowly and the response of dry aerosol particles measured; in this limit, we assume that the particles maintain an equilibrium with the RH at all times and sufficient time is allowed for the crystalline particles to transform to a solution phase once the deliquescence RH is reached, i.e. the correspondence between the water content of the deposited particles and the gas phase RH was recorded as a reference. Then, the deposited aerosol particles were dried and an RH change using a more rapid pulse sequence was performed; again, the correspondence between water content and RH was recorded and compared to the reference measurement. Consistency between these two methods for measuring the hygroscopic response could then be taken as confirmation that the RH trends generated over very short time frames and measured by the FTIR were accurate and consistent with expectations from the more gradual equilibrium state measurements. Alternatively, any delayed response in the condensed phase composition might be considered indicative of dissolution kinetics that proceed slower than the timescale for the RH change.

$NaNO_3$, NH_4NO_3 and $MgCl_2$ were chosen as sample crystalline aerosol because their deliquescence RHs vary widely with values of 75%, 63% and 32%, respectively. In Figure 5(a), we report the time-dependencies of the RH for the hygroscopic response measurements performed under both fast and slow changes in RH for the three inorganic benchmark aerosols. For example, for $NaNO_3$, the RH was increased from 0 to 80% in ~1000 s during a slow RH change measurement; during the pulsed RH change, it only took 5 s to increase the RH from 0 to 80%, with most of the transition in RH occurring over a timescale < 1 s. The variations of water content (measured from the integrated condensed phase IR band in the spectrum) with RH (from a gas phase absorption line) are shown in Figure 5(b). In each measurement, the water band area at different RHs was divided by that at the highest RH to normalize the water content to 1. The correspondence between the water content/RH relationship from the slow RH change and rapid RH change measurements is remarkable and the deliquescence RHs are within ±1%. The results for crystalline particles of NH_4NO_3 and $MgCl_2$ are similar. Not only do these results demonstrate that we can accurately measure the RH in-situ with a time resolution of 0.12 s, even when the RH change is as fast as 60% per second, they also confirms that the response in particle composition

to RH change for these three inorganic systems starting as crystalline particles is extremely rapid. Further, we illustrate in Figure 5(c) that for $NaNO_3$, NH_4NO_3 and $MgCl_2$, the timescale for deliquescence during the rapid RH change is less than ~1 s. The fast dissolution process can be captured with high resolution and confirms that deliquescence is an extremely rapid process, occurring on a timescale that is at least as short as that set by our instrumental limit (~1 s). Thus, we conclude that dissolution of atmospheric aerosol particles can be assumed to be instantaneous provided the RH increases above the deliquescence RH of the aerosol and, thus, is always rapid in the activation of cloud condensation nuclei.[49,50]

3.3 Hygroscopicity of sucrose aqueous droplets

In our experiment, the ambient RH was kept constant at 65% for 30 minutes after sucrose aqueous droplets were prepared to allow droplets to equilibrate to the gas phase. Then, the RH was controlled with step-wise decreases and increases, shown as dark cyan line in Figure 6(a), and FTIR spectra were collected synchronously. Each step in RH was followed by a constant RH for 30-180 minutes to allow the droplets compositions to equilibrate. The real time RH was calculated as described in section 2.3.

During the humidity cycles, the mass of solute (sucrose) remains constant, so the droplet mass change comes entirely from the absorption/desorption of water from the particle. In FTIR spectra, the integrated intensity of the water bending vibrational band, $\bar{A}$, is proportional to the water content of the aerosol by mass (or number of moles) according to Beer-Lambert's law.[51] Thus, it is not difficult to relate the change in mass growth factor (GF) of the deposited droplets to the change in integrated intensity, $\bar{A}$, by

$$\frac{GF_{RHa}-1}{GF_{RHb}-1}=\frac{\bar{A}_{RHa}}{\bar{A}_{RHb}} \qquad (6)$$

where $\bar{A}_{RHa}$ and $\bar{A}_{RHb}$ are $\bar{A}$ at RHa and RHb, and GF_{RHa} and GF_{RHb} are equilibrated droplets mass growth factor at *RHa* and *RHb*.

The mass growth factor at 65 % RH, $GF_{RH65\%}$, was determined from literature models as shown in Figure 6(b), using the models of Norrish (by transform w/w % water into *GF*)[52] and Zobrist et al.[34] where

$$a_w(298.15\ K, w)=\frac{(1+aw)}{(1+bw+cw^2)} \qquad (7)$$

a_w is the water activity, w is mass concentration ($g\cdot L^{-1}$), $a=-1,\ b=-0.99721,\ c=0.13599$.

Then, the GF at any RH was inferred from

$$GF_{RH} = \left[\frac{\bar{A}_{RH}}{\bar{A}_{RH65\%}}(GF_{RH65\%} - 1)\right] + 1 \quad (8)$$

At the end of each RH step, the mass growth factors are compared with equilibrate predictions in Figure 6(b) estimated from the Norris and Zobrist et al.[34] models. For RHs above the glass transition (~25% RH), our experimental data overlap with estimations from the literature. Below the glass transition (<RH 25%), the mass growth factors are higher than equilibrium predictions, indicating that the particles do not reach an equilibrated state on the timescale of the measurement.

3.4 Calculating water diffusion coefficients in sucrose aqueous droplets

The characteristic relaxation time (τ) for the composition or radius of a droplet following a step change in RH has been shown to reflect the timescale for bulk phase water diffusion in amorphous particles.[53] In a heterogeneous system consisting of domains of widely varying viscosity and diffusivity, such as the ultra-viscous or glassy aerosol particles described above, the timescales for relaxation can vary over several orders of magnitude. Thus, although in any single environment the relaxation can usually be represented by single exponential behaviour, the relaxation can be strongly non-exponential over the full macroscopic ensemble of domains. Recently, Rickards et al.[53] reported that the relaxation of viscous droplets following a perturbation in the environmental RH can be described by the Kohlrausch–Williams–Watts (KWW) response function, a stretched exponential.[54] The time-dependent response in size or composition, quantified by the function, *H(t)*, can be expressed as:[25]

$$H(t) \approx exp[-(t/\tau)^{\beta}] \quad (9)$$

where τ is a time constant and β reflects the degree of heterogeneity in the relaxation kinetics appearing as the degree to which the shape of the exponential relaxation is stretched at long times after the perturbation. In analogous manner to previous measurements of evolving size,[53] here we fit the time dependent mass growth factor of sucrose aqueous droplets following a change in environmental RH to the KWW equation to estimate the characteristic time (τ). Specifically, the time-dependence is fit to the equation:

$$GF(t) \approx GF(\infty) + [GF(0) - GF(\infty)]exp[-(t/\tau)^{\beta}] \quad (10)$$

Here $GF(\infty)$ is the equilibrated mass growth factor at the environmental RH, which can be

calculated from the thermodynamic model of Zobrist et al.[34] $GF(0)$ is the growth factor at time zero, the time when the RH reaches the final RH during a RH step, assuming that the RH change is much faster that the timescale for the compositional change. Figure 7 shows an example for an RH step from 39% to 32%.Further, we define the deviation from the expected instantaneous GF dependence as

$$Deviation = \frac{GF_{expt} - GF_{Zobrist}}{GF_{Zobrist}} \times 100\% \quad (11)$$

to characterize the degree of deviation from the fully equilibrated state. As we can see, in the first 20 seconds, as the RH decreases, the deviation increases. Growth factor during this period of time cannot be fitted by the KWW equation since droplets experience a continuously changing gas phase composition. Our experimental set up allows the RH to reach a steady RH in a short time scale. In Figure 7 we illustrate a RH drop from 39% to 32% in less than 20 s. This timescale is negligible when compared to the time scale required for such highly viscous droplets to reach equilibrium in composition, e.g. more than 2000 seconds after the RH jumped from 39% to 32%. By contrast, for dilute droplets, the time scale of RH change can be comparable with the timescale for a droplet to equilibrate, e.g. the first two RH steps in Figure 6(a). In this situation, time zero was the time when the RH started to change rapidly; the characteristic time τ obtained from the fitted curve is less accurate for these fast processes than for processes involving viscous droplets. All the fitted curves were shown in the Supplementary Information and the fitted parameters are reported in the Table 1. In order to evaluate the differences of fitting results from variable β, we also illustrate the fitted parameters when β is set as 1 in Table S1 in the Supplementary Information to show the effect of varying β on τ. It is noted that the difference between τ estimated with or without a limitation of β=1 (equivalent to single exponential) is less than 10 %.

The characteristic times recorded in this work are shown in Figure 8. The rate of RH change can be up to 60 % s^{-1}, but is not always driven this fast; much more accurate smaller changes in RH are required rather than such high rates when measurements are performed with viscous particles, where the viscosity changes very steeply with RH. The trend in τ is qualitatively consistent with the significant rise in viscosity and expected equilibration times associated with selected RH changes. In the high RH/dilute solute limit, τ approaches the value of ~1 s, indicating

fast water transport through the droplet-gas interface and the droplet bulk. τ increases significantly with decrease in RH as the droplet progresses to an ultra-viscous liquid and eventually to a glassy state, exhibiting slower response in size compared to the response of RH. A larger step in RH requires a longer time for the size to change. Measurements of condensation and evaporation rates between common RH ranges show that the τ is smaller for condensation than for evaporation. A similar observation has been observed when comparing the evaporation and condensation kinetics for water in ultra-viscous and glassy aerosol: loss of water from a viscous particle is slower than the dissolution of a viscous core into a condensing lower viscosity shell.[55]

In Figure 8(b), different colour circles represent time-constants determined from different step changes in RH. Our measurements are based on the relaxation time of droplets following an RH jump where the relaxation time constant is the τ defined by the KWW equation. During relaxation, the concentration of sucrose or water in the condensed phase particles continuously changes; measured time constants can be expected to be more reliably reported at a fixed RH when the RH jump is only over a small range. The RH jump in experiment 1 is smaller than in experiment 2, as seen in Table 1, and, thus, the time constants from experiment 1 can be more reliably reported at a fixed RH. Compared to experiment 1 and 2, the sucrose concentration is lower as the RH is higher in experiment 3. Thus, the RH change induced was faster, and the time resolution of FTIR spectra was set as 0.12 s, higher than the 3.4 s used in experiment 1 and 2.

Given the complexities of fully accounting for the particle size distribution and the non-sphericity of the deposited particles, we do not make any attempt here to provide a rigorous model of the water diffusion kinetics. Instead, we compare the time-constants from our measurements with diffusional mixing timescales derived from previous measurements of diffusion constants provided by Price et al.[38-40] and Zobrist et al.[34] In these predictions, we use the diffusion coefficient estimated from these previous parameterizations at the final RH of the measurement, the RH at which the deposited aerosols are relaxing in composition. The relationship between the diffusion constant and characteristic relaxation time due to diffusional mixing is

$$\tau = \frac{r^2}{\pi^2 D} \qquad (12)$$

where r is the droplet radius, D is the diffusion coefficient and τ is the characteristic time.[56]

The droplet radius used in this estimation is 3 μm, as shown in Figure 2(a). Excellent consistency is observed. Predictions based on the viscosities reported by Power et al[35] and the Stokes-Einstein equation are also shown. As the sucrose molecule is much larger than water, it is reasonable that the binary diffusion constant will be several orders of magnitude higher than estimated from this relationship when water is diffusing in a highly viscous or semi-solid organic matrix.[24,57] He et al[58] derived the water self-diffusion coefficient from the free-volume model. Their results are close to the results of Price et al,[38-40] Zobrist et al[34] and this work at RH higher than 40%, but deviate from these results by several orders of magnitude at RH of 10% which is the RH that glassy state form. A possible reason is that the calculation of water self-diffusion coefficient in the free-volume model is based on the change of the droplet volume, which is less suitable for high viscous or semi-solid bulk phase, when the particle volume is not so sensitivity to water transportation in the bulk phase.

The correspondence between the measurements of relaxation timescales reported here and estimates of diffusional mixing timescales using previously published diffusion constants the simple use of equation (12), is striking. The comparison suggests the validity of a rather simple method for estimating the binary diffusion constants using the time-constant from fitting the relaxation kinetics following the RH change. Although we use the KWW equation here, the relaxation kinetics could have been fit to a single exponential[53] or just a half-time[55] as used in previous work; these different representations change very little the reported time-constant for the process although they provide varying levels of accuracy in representing the time-dependence.[53] We use the KWW equation here as we consider that it provides a more accurate method for representing the kinetics of the mass transfer process. The consistency found empirically between measured time constants and estimates using the diffusion constant at the final RH of the perturbation suggests that the rate limiting process for the equilibration is always governed by how fast water exchange can occur between the near surface region of the particle and the gas phase. In the very high drying rates that can be achieved in these measurements, the step down in RH leads to a step in water activity at the droplet surface that is so fast that all subsequent mass transfer is governed by diffusion through this dry outer shell, very similar to typical observations of evaporation rates when droplet drying occurs at high Peclet numbers. Then, the subsequent slow relaxation in composition can be correlated with the diffusion constant of water through this outer

viscous shell at fixed composition. When considering the complexities of modelling slow transport in atmospheric aerosol, this observation could provide some justification for using simple models of equilibration timescale using bulk diffusivities at a single water activity and equation (12) rather than modelling the full microphysical detail and heterogeneity at the single particle level.[59,60]

4. Conclusion

Highly viscous and glassy aerosol particles are considered to occur widely in the atmosphere, particularly for the organic aerosol fraction. Their physical and chemical properties are affected by the kinetics of the interaction with environmental water vapour and other chemical species. Studies of molecular diffusion process in highly viscous and glassy aerosol particles are important for better characterization of aerosol equilibration timescales in the atmosphere. Here we report a new method to evaluate the water transport kinetics in particles of varying phase and viscosity using Rapid scan FTIR spectroscopy and a home-made pulse RH controlling system. The RH was derived from the band intensities in the IR spectra and Rapid scan FTIR spectroscopy offered a time resolution as high as 0.12 s. The high RH change velocity, high time resolution of spectral acquisition and real time RH measurement ensure that this method is accurate over a wide solution concentration range. Using this method, we demonstrate the dissolution timescales of crystalline particles are rapid, occurring on a timescale shorter than the timescale for the RH change (<1 s). Further, we explore the relaxation process of sucrose aqueous droplets following a step in RH to characterise the timescale for mass transfer in amorphous and viscous particles. Measurements of water transfer characteristic timescales in sucrose aqueous droplets are reported spanning 4 orders of magnitude, from the liquid to the glassy state. The consistency between estimated timescales for relaxation in particle composition from accurate parameterisations of diffusion constants and the empirical time-constants reported here, suggest that the microphysical detail of mass transport and equilibration timescales in viscous particles can, to a first approximation, be justifiably neglected when estimating relaxation timescales for ambient particles and that a single gas phase RH can be used to estimate relaxation timescale.

Acknowledgments

YZ and CC contributed equally to this work and should be considered as co-first authors. SFP acknowledges support from the National Natural Science Foundation of China (No. 21373026; No.

91644101). JPR acknowledges the Natural Environment Research Council for support through grant NE/M004600/1. YHZ acknowledges support from the National Natural Science Foundation of China (No. 21473009; No. 41175119; No. 91544223).

References:

1. R. J. Charlson, S. E. Schwartz, J. M. Hales, R. D. Cess, J. A. Coakley, Jr., J. E. Hansen and D. J. Hofmann, *Science*, 1992, **355**, 423.
2. A. Nenes, S. Ghan, H. Abdul-Razzak, P. Y. Chuang and J. H. Seinfeld, *Tellus B*, 2001, **53**, 133-149.
3. J. E. Penner, M. Andreae and M. Annegarn, Aerosols, their direct and indirect effects, in Climate Change 2001: The Scientific Basis. Contribution of Working Group I to the Third Assessment Report of the Intergovernmental Panel on Climate Change., Cambridge University Press, 2001.
4. U. Lohmann and J. Feichter, *Atmos. Chem. Phys.*, 2005, **5**, 715-737.
5. Z. Levin and W. R. Cotton, Aerosol pollution impact on precipitation: a scientific review, Springer, 2009.
6. J. Walker, J. Wills and J. Reid, *Weather*, 2011, **66**, 165-168.
7. U. Pöschl, *Angew. Chem.-Int. Edit.*, 2005, **44**, 7520-7540.
8. D. Sinclair, R. J. Countess and G. S. Hoopes, *Atmos. Environ.*, 1974, **8**, 1111-1117.
9. J. W. Fitzgerald, *Appl. Optics.*, 1984, **23**, 411-418.
10. I. N. Tang, *J. Geophys. Res. Atmos.*, 1996, **101**, 19245-19250.
11. B. Ervens, B. J. Turpin and R. J. Weber, *Atmos. Chem. Phys. Dis.*, 2011, **11**, 22301-22383.
12. B. Ervens, Y. Wang, J. Eagar and W. R. Leaitch, *Atmos. Chem. Phys.*, 2012, **12**, 33083-33125.
13. A. S. Wexler and S. L. Clegg, *J. Geophys. Res. Atmos.*, 2002, **D14**, 11-14.
14. S. L. Clegg and P. Brimblecombe, *J. Phys. Chem. A*, 1998, **12**, 2155-2171.
15. A. Zuend, C. Marcolli, B. P. Luo and T. Peter, *Atmos. Chem. Phys.*, 2008, **8**, 4559-4593.
16. A. Zuend, C. Marcolli, A. M. Booth, D. M. Lienhard, V. Soonsin, U. K. Krieger, D. O. Topping, G. Mcfiggans, T. Peter and J. H. Seinfeld, *Atmos. Chem. Phys.*, 2011, **11**, 9155-9206.
17. S. L. Clegg and A. S. Wexler, *J. Phys. Chem. A*, 2011, **115**, 3393-3460.
18. T. Lei, A. Zuend, W. G. Wang, Y. H. Zhang and M. F. Ge, *Atmos. Chem. Phys.*, 2014, **14**, 11625-11663.
19. F. H. Marshall, R. E. H. Miles, Y. C. Song, P. B. Ohm, R. M. Power, J. P. Reid and C. S. Dutcher, *Chem. Sci.*, 2015, **7**, 1706-1710.
20. J. L. Jimenez, M. R. Canagaratna, N. M. Donahue, A. S. Prevot, Q. Zhang, J. H. Kroll, P. F. Decarlo, J. D. Allan, H. Coe and N. L. Ng, *Science*, 2009, **326**, 1525-1529.
21. M. Hallquist, J. C. Wenger, U. Baltensperger, Y. Rudich, D. Simpson, M. Claeys, J. Dommen, N. M. Donahue, C. George and A. H. Goldstein, *Atmos. Chem. Phys.*, 2009, **9**, 5155-5236.

22. B. Zobrist, C. Marcolli, D. A. Pedernera and T. Koop, *Atmos. Chem. Phys.*, 2008, **8**, 9263-9321.
23. E. Mikhailov, S. Vlasenko, T. Koop and U. Poschl, *Atmos. Chem. Phys.*, 2009, **9**, 9491-9522.
24. M. Shiraiwa, A. Zuend, A. K. Bertram and J. H. Seinfeld, *Phys. Chem. Chem. Phys.*, 2013, **15**, 11441-11453.
25. T. Koop, J. Bookhold, M. Shiraiwa and U. Pöschl, *Phys. Chem. Chem. Phys.*, 2011, **13**, 19238-19255.
26. P. Koepke, Global aerosol data set, Max-Planck-Institut für Meteorologie, Hamburg, Germany, 1997.
27. M. Kanakidou, J. H. Seinfeld, S. N. Pandis and I. Barnes, *Atmos. Chem. Phys.*, 2004, **5**, 1053-1123.
28. M. D. Petters and S. M. Kreidenweis, *Atmos. Chem. Phys.*, 2013, **13**, 1081-1091.
29. F. Yu, G. Luo and X. Ma, *Atmos. Chem. Phys.*, 2012, **12**, 93-128.
30. S. H. Chung and J. H. Seinfeld, *J. Geophys. Res. Atmos.*, 2002, **107**, 11-14.
31. X. Liu and J. Wang, *Environ. Res. Lett.*, 2010, **5**, 44010.
32. N. Hodas, A. Zuend, W. Mui, R. C. Flagan and J. H. Seinfeld, *Atmos. Chem. Phys.*, 2015, **15**, 5027-5045.
33. M. K. Kuimova, S. W. Botchway, A. W. Parker, M. Balaz, H. A. Collins, H. L. Anderson, K. Suhling and P. R. Ogilby, *Nat. Chem.*, 2009, **1**, 69-73.
34. B. Zobrist, V. Soonsin, B. P. Luo, U. K. Krieger, C. Marcolli, T. Peter and T. Koop, *Phys. Chem. Chem. Phys.*, 2011, **13**, 3514-3526.
35. R. M. Power, S. H. Simpson, J. P. Reid and A. J. Hudson, *Chem. Sci.*, 2013, **4**, 2597-2604.
36. J. W. Lu, A. M. J. Rickards, J. S. Walker, K. J. Knox, R. E. H. Miles, J. P. Reid and R. Signorell, *Phys. Chem. Chem. Phys.*, 2014, **16**, 9819.
37. S. Bastelberger, U. K. Krieger, B. P. Luo and T. Peter, *Atmos. Chem. Phys. Discuss.*, 2017, doi:10.5194/acp-2017-210.
38. H. C. Price, B. J. Murray, J. Mattsson, D. O'Sullivan, T. W. Wilson, K. J. Baustian and L. G. Benning, *Atmos. Chem. Phys.*, 2014, **14**, 3817–3830.
39. H. C. Price, J. Mattsson and B. J. Murray, *Phys. Chem. Chem. Phys.*, 2016, **18**, 19207-19216.
40. H. C. Price, J. Mattsson, Y. Zhang, A. K. Bertram, J. F. Davies, J. W. Grayson, S. T. Martin, D. O'Sullivan, J. P. Reid and A. M. Rickards, *Chem. Sci.*, 2015, **6**, 4876-4883.
41. J. F. Davies and K. R. Wilson, *Anal. Chem.*, 2016, **88**, 2361–2366.
42. D. M. Lienhard, A. J. Huisman, U. K. Krieger, Y. Rudich, C. Marcolli, B. P. Luo, D. L. Bones, J. P. Reid, A. T. Lambe and M. R. Canagaratna, *Atmos. Chem. Phys.*, 2015, **15**, 24473-24511.
43. J. W. L. Lee, V. Carrascon, P. J. Gallimore, S. J. Fuller, A. Bjorkegren, D. R. Spring, F. D. Pope and M. Kalberer, *Phys. Chem. Chem. Phys.*, 2012, **14**, 8023–8031.
44. N. A. Hosny, C. Fitzgerald, C. Tong, M. Kalberer, M. K. Kuimova and F. D. Pope, *Faraday Discuss.*, 2013, **165**, 343.
45. L. Rkiouak, M. J. Tang, J. C. J. Camp, J. McGregor, I. M. Watson, R. A. Cox, M. Kalberer, A.

D. Ward and F. D. Pope, *Phys. Chem. Chem. Phys.*, 2014, **16**, 11426–11434.

46. N. A. Hosny, C. Fitzgerald, A. Vysniauskas, A. Athanasiadis, T. Berkemeier, N. Uygur, U. Poschl, M. Shiraiwa, M. Kalberer, F. D. Pope and M. K. Kuimova, *Chem. Sci.*, 2015, **7**, 1357–1367.
47. C. B. Leng, S. F. Pang, Y. Zhang, C. Cai, Y. Liu and Y. H. Zhang, *Environ. Sci. Technol.*, 2015, **49**, 9107-9115.
48. M. A. Ottenhof, W. Macnaughtan and I. A. Farhat, *Carbohyd. Res.*, 2003, **338**, 2195-2202.
49. L. T. Padro, A. Asa-Awuku, R. Morrison and A. Nenes, *Atmos. Chem. Phys.*, 2007, **7**, 5263–5274.
50. N. C. Shantz, R. Y.-W. Chang, J. G. Slowik, A. Vlasenko, J. P. D. Abbatt and W. R. Leaitch, *Atmos. Chem. Phys.*, 2010, **10**, 299–312.
51. Y. Liu, Z. Yang, Y. Desyaterik, L. G. Paul, H. Wang and A. Laskin, *Anal. Chem.*, 2008, 80, 633-642.
52. R. S. Norrish, *Inter. J. Food Sci. Technol.*, 1966, **1**, 25-39.
53. A. M. Rickards, Y. C. Song, R. E. Miles, T. C. Preston and J. P. Reid, *Phys. Chem. Chem. Phys.*, 2015, **17**, 10059-10073.
54. M. D. Ediger, *Annu. Rev. Phys. Chem.*, 2000, **51**, 99-128.
55. D. L. Bones, J. P. Reid, D. M. Lienhard, and U. K. Krieger, *Proc. Nat. Aca. Sci.*, 2012, **109**, 11613-11618.
56. J. H. Seinfeld, S. N. Pandis, J. H. Seinfeld and S. N. Pandis, Atmospheric chemistry and physics: from air pollution to climate change., Wiley, 1998.
57. L. Zhu, T. Cai, J. Huang, T. C. Stringfellow, M. Wall and L. Yu, *J. Phys. Chem. B*, 2011, **115**, 5849-5855.
58. X. He, A. Fowler and M. Toner, *J. Appl. Phys.*, 2006, **100**, 74702.
59. M. Shiraiwa and J. H. Seinfeld, *Geophys. Res. Lett.*, 2012, **39**, 24801.
60. S. O'Meara, D. O. Topping and G. Mcfiggans, *Atmos. Chem. Phys.*, 2016, **16**, 1, 1-25.

Table 1. KWW function fitted parameters of RH steps and the diffusion coefficient of water.

RH / %	***τ / s***	***β***	***R^2***	***D_{H2O} / $m^2 s^{-1}$***
	Experiment 1			
61-56	12	0.97	0.987	7.6×10^{-14}
56-50	20	0.83	0.973	4.6×10^{-14}
44-38	198	0.56	0.949	4.6×10^{-15}
39-32	131	1	0.976	7.0×10^{-15}
32-26	341	0.76	0.995	2.7×10^{-15}
26-20	939	0.71	0.993	9.7×10^{-16}
20-13	2811	0.63	0.983	3.2×10^{-16}
13-0	4790	0.72	0.996	1.9×10^{-16}
0-22	743	0.65	0.999	1.2×10^{-15}
22-45	39	3.42	0.995	2.3×10^{-14}
48-0	868	0.58	0.999	1.1×10^{-15}
	Experiment 2			
59-52	7	1.1	0.996	1.3×10^{-13}
38-30	80	0.84	0.992	1.1×10^{-14}
30-18	472	0.51	0.993	1.9×10^{-15}
18-0	3448	0.79	0.997	2.6×10^{-16}
	Experiment 3			
58-72	0.6	0.68	0.989	1.5×10^{-12}
48-64	0.55	0.84	0.992	1.6×10^{-12}

Figure 1. Experimental set-up of vacuum FTIR setup.

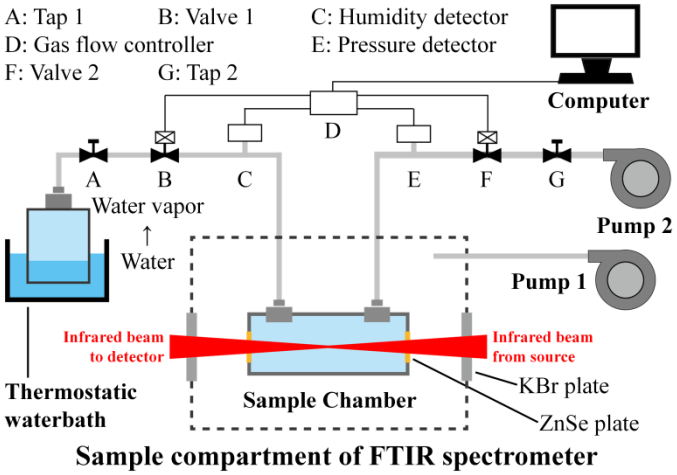

Figure 2. Illustration of (a) bright-field images, (b) number percentage, (c) mass percentage and (d) absorption area percentage of droplets with different sizes deposited on the substrate.

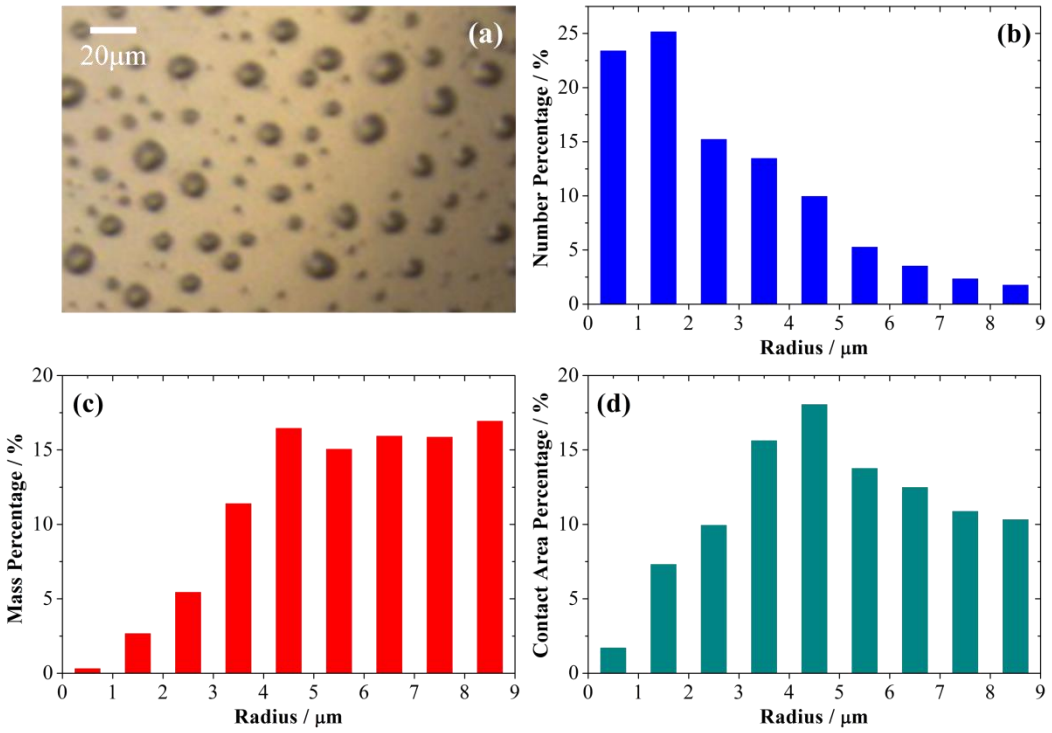

Figure 3. (a) Offset water vapour spectra (1820-1880 cm^{-1}) over a range in vapour pressure and RH estimated from the value of the water partial pressure. (b) Absorbance at 1844.2 cm^{-1} (black filled square) as a function of RH calculated from p (black dashed line). The slope of fitted line in (b) is $2.866 \pm 0.007 \times 10^{-4}$ and $R^2 = 0.9995$.

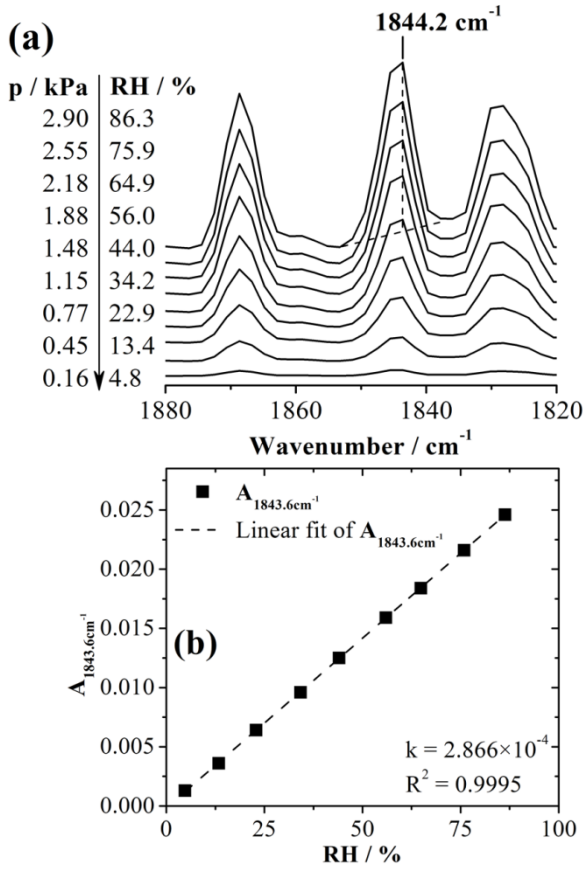

Figure 4. FTIR spectra of sucrose aerosol particles at various RHs (black: RH=0 % for 24 h; red: RH = 1 % for 24 h; blue: RH = 40 %; purple: RH = 60 %; olive: RH = 77 %). (A) Comparison of total spectrum (both gas phase and condensed phase shown by black line) and spectrum of condensed phase only (once gas phase lines have been subtracted, blue line). (B) Expanded view of gas phase line used in the calibration and estimation of RH. (C) Expanded view of the condensed phase band used to determine the water content of the particles once the gas phase lines have been subtracted.

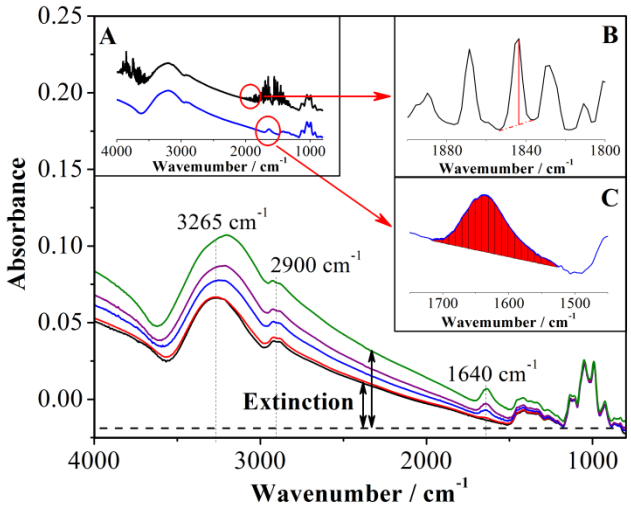

Figure 5. (a) Time dependence in the RH retrieved from the vapor phase FTIR measurements for $NaNO_3$ (square), NH_4NO_3 (circle) and $MgCl_2$ (triangle) aerosol particle measurements under slow RH change (filled points) and pulse RH change (opened points). (b) Normalized water content determined for each aerosol sample for the RH trajectories shown in (a). Filled points and opened points represent the results of the different experiments reported in (a). (c) Correlation between Normalized water content determined for each aerosol sample in (b) and experimental time in (a).

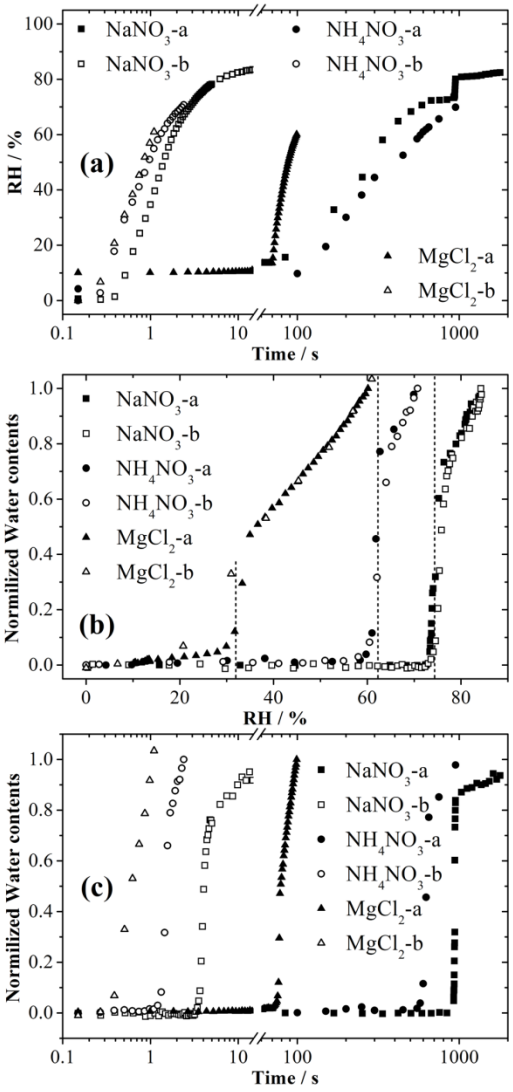

Figure 6. (a) Time dependence of the mass growth factor (blue line, this work; red line, calculated from Zobrist's model;[34] black line, calculated from Norrish's model[52]) and RH (dark cyan line). (b) A comparison of measured mass growth factor (blue points, two sets of experiments in this work) versus RH with equilibrated predictions assuming the models of Norrish[52] (black line) and Zobrist et al (red line).[34]

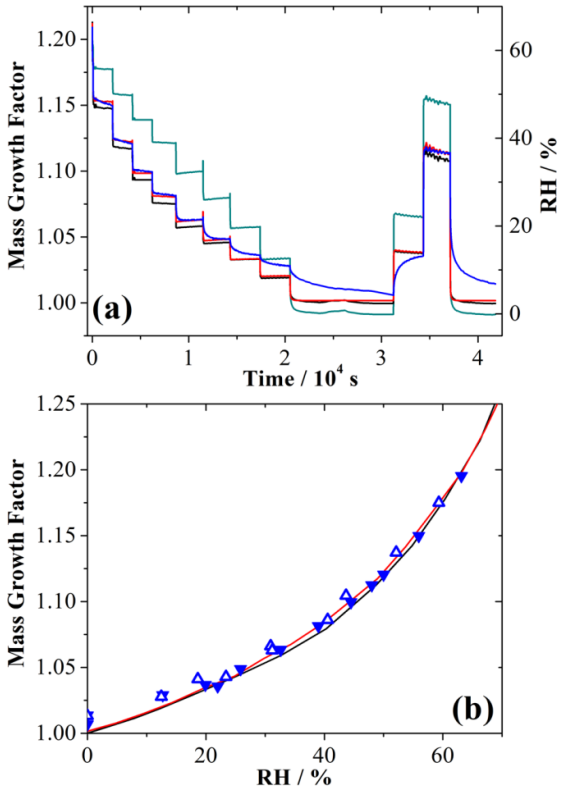

Figure 7. (a) A comparison of the expected time-dependence of the mass growth factor following an RH step from 39% to 32% (from the model of Zorbrist et al.,[34] black opened square), the measured mass growth factor inferred from the water band area (black filled square) and the deviation (red filled circle) . (b) The time-dependence in the sucrose mass growth factor curve and the corresponding KWW fit for the data shown in (a).

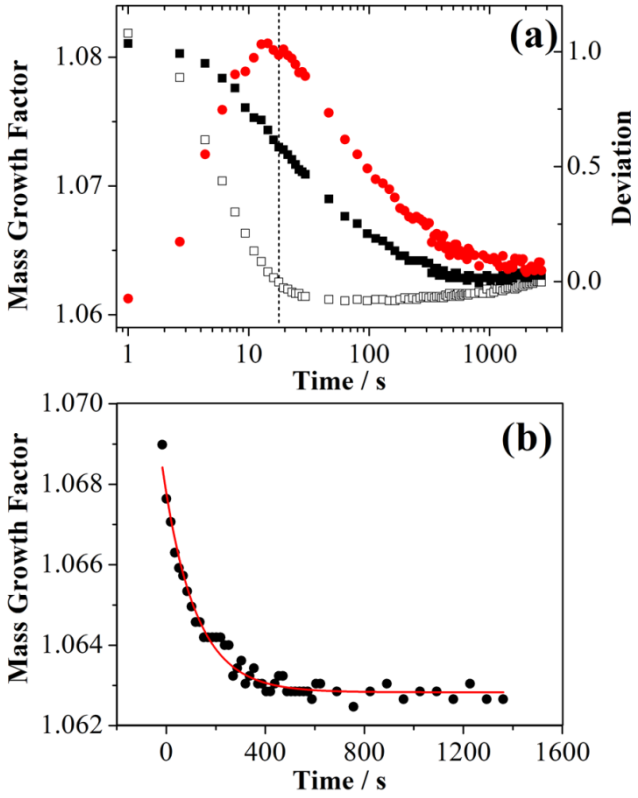

Figure 8. Characteristic time for changes in size of sucrose droplet from vacuum FTIR measurements presented in two different ways. In (a), different colours represent the characteristic time, whilst in (b), different colours represent different RH steps. Characteristic time constants are also shown derived from diffusion coefficient of water in sucrose aqueous droplets from Price et al.[38-40] (black opened triangles), Zobrist et al.[34] (black short dotted line), He et al.[58] (black solid line) and using the Stokes-Einstein equation and the viscosity data of Power et al.[35] (black opened circles).